A&A 375, 1018–1031 (2001)
DOI: 10.1051/0004-6361:20010896

Astronomy & Astrophysics

An interferometric study of the HH 288 molecular outflow⋆

F. Gueth[1,2], P. Schilke[1], and M. J. McCaughrean[3]

[1] Max-Planck-Institut für Radioastronomie, Auf dem Hügel 69, 53121 Bonn, Germany
[2] Institut de Radio Astronomie Millimétrique, 300 rue de la Piscine, 38406 Saint Martin d'Hères, France
[3] Astrophysikalisches Institut Potsdam, An der Sternwarte 16, 14482 Potsdam, Germany

Received 29 January 2001 / Accepted 18 June 2001

Abstract. We present an interferometric study of the CO $J = 1 \rightarrow 0$ line emission in the HH 288 molecular outflow. The IRAM Plateau de Bure interferometer was used to obtain an 11–field mosaic covering the whole flow ($\sim$2 pc) with an angular resolution of about 3.5″ (7000 AU at a distance of 2 kpc). The data were complemented with short-spacings derived from IRAM 30–m observations. The exciting source of HH 288, IRAS 00342+6347, is a young (dynamical age of the outflow $\simeq$a few 10^4 years) intermediate-mass (bolometric luminosity $\simeq$500 $L_\odot$, envelope mass $\simeq$6 to 30 $M_\odot$) embedded protostar. This source is likely to be an intermediate-mass counterpart of a classical Class 0 low-mass protostar. HH 288 is actually a quadrupolar outflow, and the angular resolution provided by the interferometric observations allows us to rule out models involving limb-brightened walls of a wide-angle single flow to explain such a morphology. The presence of two protostars in the central condensation is the most appealing explanation to account for the presence of the two flows. While the small East-West flow has a quite simple morphology and kinematics, the large North-South flow includes several overlapping structures, created by successive ejection events. Large collimated limb-brightened cavities are observed, with high-velocity material located along or near the flow axis. The internal structure of HH 288, including morphological coincidence between the CO and H_2 emission, supports prompt entrainment at the head of large bow-shocks as the main formation process of molecular outflows from intermediate-mass protostars.

Key words. stars: formation – interstellar medium: individual objects: HH 288 – interstellar medium: jets and outflows – interstellar medium: molecules – radio lines: ISM

1. Introduction

The molecular outflows driven by *low-mass* protostars have been extensively studied during the last few years, giving rise to a detailed description of their physical properties (see e.g. the recent reviews by Bachiller 1996; Richer et al. 2000; Bachiller & Tafalla 2000). The current picture of the outflow formation process involves ejection of matter from a magnetized accretion disk (e.g. Shu et al. 1995; Ferreira & Pelletier 1995); the jet/wind that is created interacts with the ambient interstellar medium to create a molecular outflow (see Cabrit et al. 1997, and references therein). The nature of the actual entrainment mechanism is still debated (Cabrit et al. 1997) but recent wide-field H_2 and millimetre interferometric observations provide increasing evidence that the outflowing gas corresponds to the wake of large bow-shocks, which are disturbing the ambient material while travelling downstream in a protostellar jet (e.g. Bachiller et al. 1995a; Davis et al. 1998; Gueth & Guilloteau 1999).

Molecular outflows are also a common property of young *massive* protostars (Shepherd & Churchwell 1996a, 1996b). Compared to their low-mass counterparts, these outflows are much more energetic (Shepherd & Churchwell 1996a, 1996b) and have much more complex structures (e.g. Hunter et al. 1997; Shepherd et al. 1997). It remains actually unclear whether the same flow formation mechanism is at work in low- and high-mass protostars (Churchwell 2000; Richer et al. 2000). Indeed, several important factors might differ. For example, the models of accretion disks might not be appropriate for high-mass objects; the close protostellar environment, in which the outflow is propagating, has very different properties; massive objects produce strong radiation pressure and stellar wind, hence disrupting their envelope. The superposition of multiple outflows in high-mass star-forming regions can also contribute to the complex observed properties (e.g. Shepherd et al. 1997). Compared to low-mass sources,

Send offprint requests to: F. Gueth, e-mail: gueth@iram.fr

⋆ Based on observations carried out with the IRAM Plateau de Bure Interferometer. IRAM is supported by INSU/CNRS (France), MPG (Germany), and IGN (Spain).

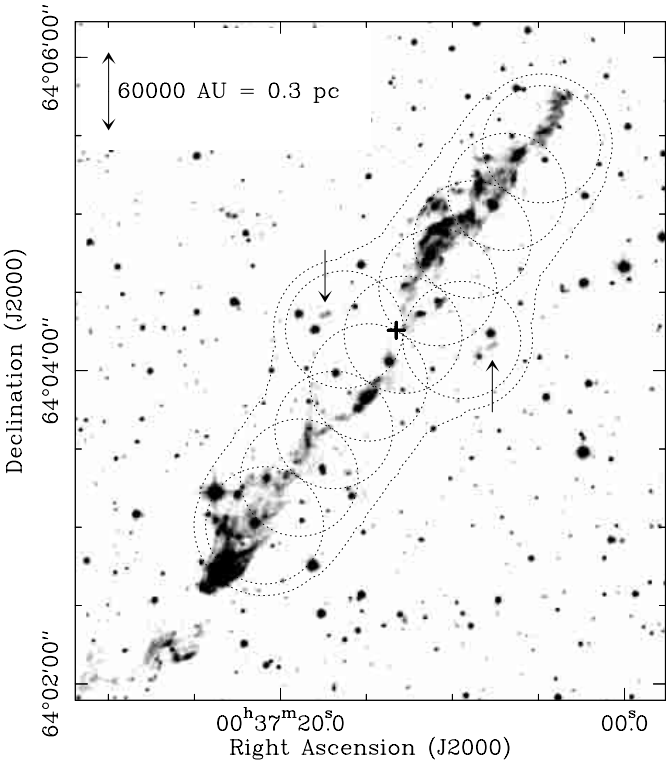

Fig. 1. H_2 $v = 1{-}0$ S(1) line at 2.12 μm + continuum emission in HH 288 observed with the Calar Alto 3.5–m telescope, with a seeing of 0.9″ FWHM (from McCaughrean & Dent 2001). The cross indicates the position of the protostellar source. The dash circles represent the 115 GHz half power primary beam width of the fields observed with the IRAM interferometer. Their combination allows us to construct a mosaic whose extent is also drawn. Note that the most southern V-shaped shock is located outside the interferometric mosaic. There is further H_2 emission roughly one parsec to the south-east of this V-shaped bow (McCaughrean & Dent 2001) that is also not covered in the present interferometric imaging. The two arrows point towards the two faint H_2 features whose positions are indicated in Fig. 9.

the study of high-mass protostars suffers from the larger distances and the shorter evolutionary timescale, which makes it difficult to probe the very earliest evolutionary stages. So far, only a few outflows driven by extremely young, deeply embedded, high-mass protostars have been studied at high-angular resolution (i.e. using millimetre interferometry), e.g. IRAS 20126+4104 (Cesaroni et al. 1997, 1999; Shepherd et al. 2000), G 192.16 (Shepherd et al. 1998), or Cepheus-A East (Gómez et al. 1999).

In this paper, we present a detailed CO $J = 1 \rightarrow 0$ interferometric study of the HH 288 molecular outflow. This object is likely to be driven by an *intermediate-mass* protostar, and we thus intend to highlight the transition between the (rather simple) low-mass protostellar outflows and the (much more complex) outflows created by high-mass sources. HH 288, also known as the Dragon Jet, is a molecular hydrogen emission outflow discovered by McCaughrean & Dent (2001). Figure 1 shows HH 288 in the 2.12 μm $v = 1{-}0$ line of H_2, which traces the shocked gas. The jet is highly collimated and shows clear bow-shock structures (as in low-mass protostellar flows) but also a complex of clumps and knots (reminiscent of high-mass flows). The exciting central source, IRAS 00342+6347, has a bolometric luminosity of a few hundred solar luminosities (Dent et al. 1998; see also Sect. 4.3), which hints at an intermediate-mass protostar. Wouterloot et al. (1993) reported the presence of two H_2O masers in the vicinity of this source. HH 288 is located in the Cepheus region; the systemic velocity of the associated molecular gas is about -29 km s^{-1}, which corresponds to a kinematical distance of $\sim$2 kpc. In addition to the presence of the Herbig-Haro jet (Fig. 1), strong ejection activity is also revealed by the presence of a large molecular outflow (McCaughrean & Dent 2001).

2. Observations

The bulk of our data consists of IRAM Plateau de Bure interferometer maps of the CO $J = 1 \rightarrow 0$ emission in HH 288. We also carried out CO $J = 1 \rightarrow 0$ and $J = 2 \rightarrow 1$ single-dish observations using the IRAM 30–m antenna.

2.1. IRAM 30–m observations

The IRAM 30–m telescope was used on 1998 April 18 and 19 to map the HH 288 outflow simultaneously in the CO $J = 1 \rightarrow 0$ and $J = 2 \rightarrow 1$ lines. The receivers were tuned single-sideband, with typical rejections of 30 dB at 115 GHz and 20 dB at 230 GHz. The system temperatures ranged from 300 to 500 K at 115 GHz, and 350 to 800 K at 230 GHz. The antenna half power beamwidth and main-beam efficiency were 23″ and 0.68 at 115 GHz, and 12″ and 0.39 at 230 GHz respectively. The backend for the CO $J = 1 \rightarrow 0$ observations was an auto-correlator providing a spectral resolution of 20 kHz ($\sim$0.05 km s^{-1}) in a 35 MHz ($\sim$90 km s^{-1}) wide interval. To analyse the CO $J = 2 \rightarrow 1$ spectra, we used a 512-channel filterbank of 1 MHz ($\sim$1.3 km s^{-1}) resolution. A region of $180'' \times 220''$, centred on the IRAS source position, was mapped using the classical position switching technique. The integration time was 20 s per point, and the sampling was 10″. The area was observed twice, with an offset of +5″ in both directions between the two maps. Hence, the resulting sampling is 7″. Note that the CO $J = 2 \rightarrow 1$ map is thus not fully sampled. Second order polynomials were subtracted from all spectra in order to get flat baselines.

2.2. IRAM Plateau de Bure observations

HH 288 was observed with the IRAM Plateau de Bure millimetre array (Guilloteau et al. 1992) in 1998 May to August. Four 15–m antennas were used in four different configurations, with baseline lengths ranging from 24 m to 181 m. To cover the whole HH 288 area, we observed an 11–field mosaic (Fig. 1). The dual-channel receivers were tuned to 115.271 GHz USB with a sideband rejection of about 5 dB and 230.538 GHz LSB in double sideband

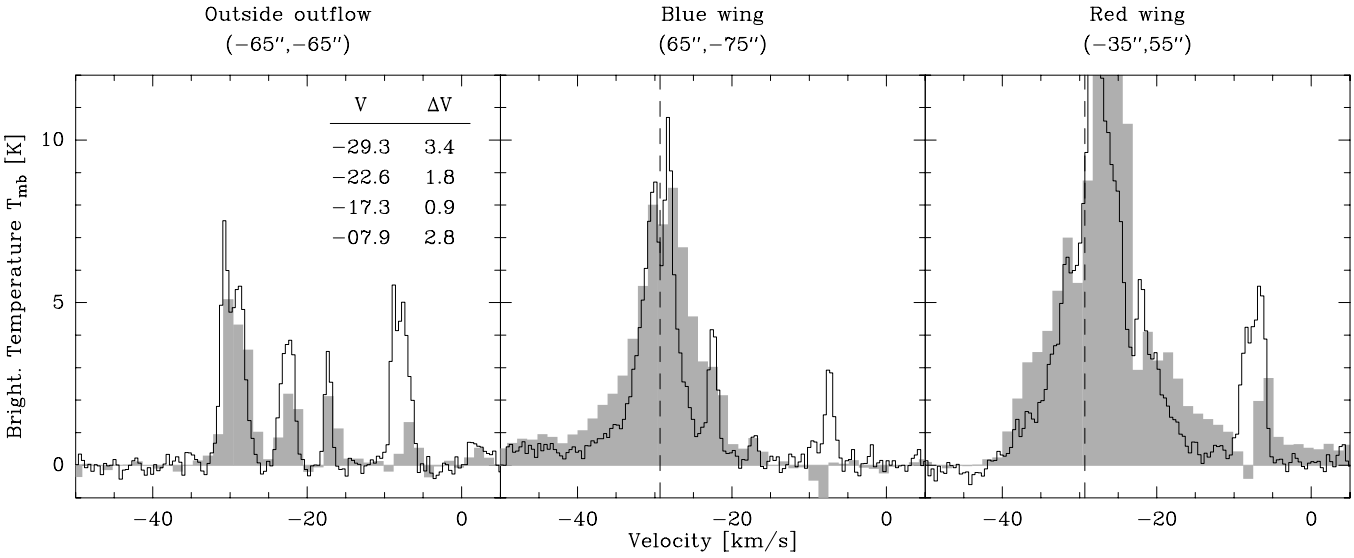

Fig. 2. Single-dish spectra of the CO $J=1\rightarrow0$ and CO $J=2\rightarrow1$ (greyscale) emission at three selected positions. The spectra were averaged in $\pm10''$ areas around the offsets (from the central source) indicated above each box. These positions are also shown in Fig. 3. Four velocity components arising from quiescent clouds are present. Gaussian fits to the CO $J=1\rightarrow0$ spectrum observed at the position free from outflow emission yield the centre velocities and FWHM widths indicated in the upper corner of the left panel. The adopted HH 288 systemic velocity, $-29\,\mathrm{km\,s^{-1}}$, is indicated by a dash vertical line in the central and right panels.

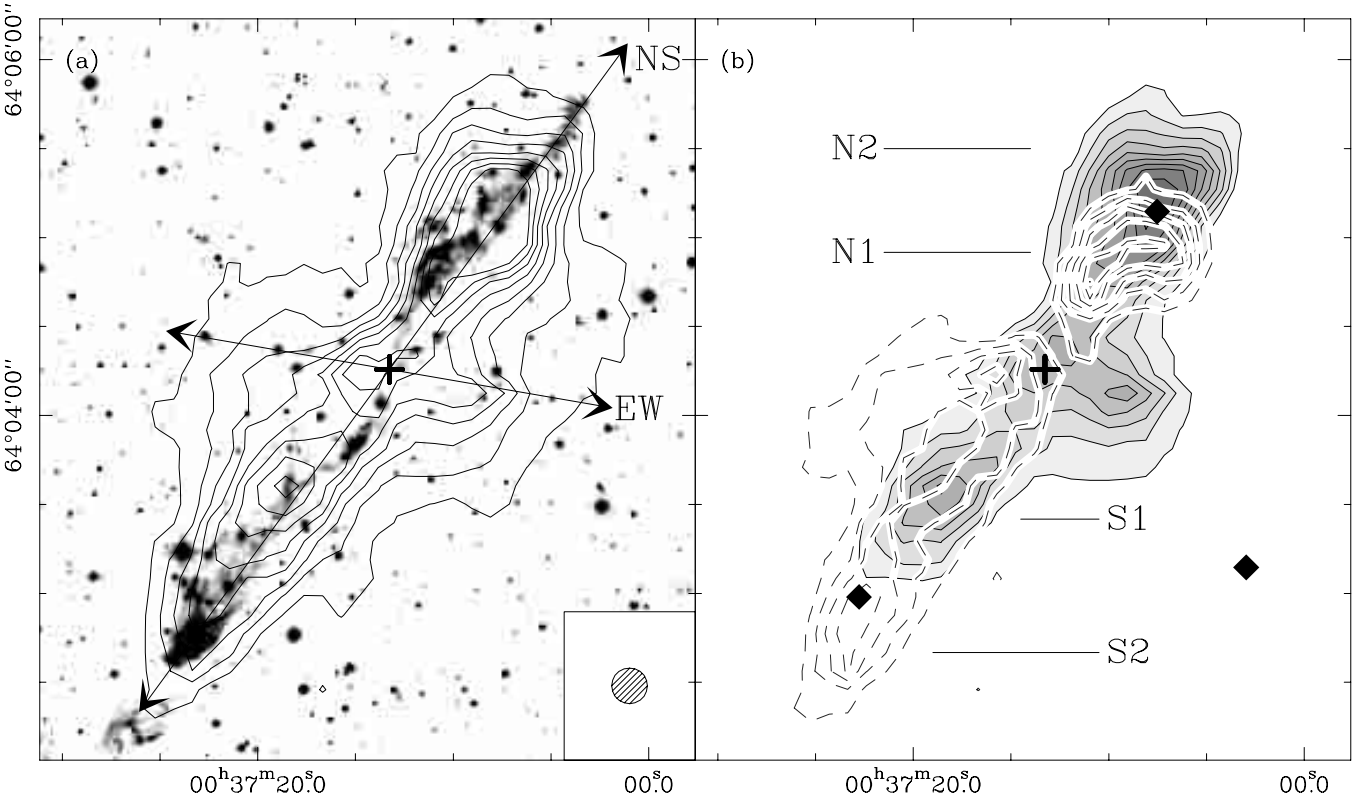

Fig. 3. CO $J=2\rightarrow1$ emission in HH 288 observed with the IRAM 30–m antenna. The angular resolution is $12''$. **a)** Integrated emission for all velocities from -67.5 to $7.5\,\mathrm{km\,s^{-1}}$, superimposed on the H_2 emission in greyscale. Contours are 15 K $\mathrm{km\,s^{-1}}$, in unit of main-beam brightness temperature. The two first contours are not plotted, because they only show very extended structures due to quiescent emission. The cross indicates the position of the exciting source, IRAS 00342+6347, and the arrows outline the axis of the two outflows detected in HH 288. **b)** Overlay of the blue-shifted (dash lines; velocities from -67.5 to $-31.5\,\mathrm{km\,s^{-1}}$; contours are 7.5 K $\mathrm{km\,s^{-1}}$, starting at 15 K $\mathrm{km\,s^{-1}}$) and red-shifted (greyscale and continuous lines; velocities from -26.5 to $7.5\,\mathrm{km\,s^{-1}}$; contours are 10 K $\mathrm{km\,s^{-1}}$, starting at 30 K $\mathrm{km\,s^{-1}}$) emission. The positions of the spectra presented in Fig. 2 are indicated by the black diamonds.

mode, to observe the CO $J=1\rightarrow0$ and $J=2\rightarrow1$ lines simultaneously. 230 GHz data were mostly unusable due to poor summer weather conditions. At 115 GHz, the typical SSB system temperature was 300 to 400 K, and the phase noise was below 30°. One correlator unit was set up to provide a channel spacing of 1.6 $\mathrm{km\,s^{-1}}$ for the CO $J=1\rightarrow0$ line, in a $\sim$200 $\mathrm{km\,s^{-1}}$ wide velocity interval, and another one provided a channel spacings of 0.2 $\mathrm{km\,s^{-1}}$ in the central 50 $\mathrm{km\,s^{-1}}$. Two other units were used in broad-band mode, to allow continuum measurements at 115 GHz (2.6 mm) over a 320 MHz wide interval. Temporal fluctuations of the amplitude and phase were calibrated with frequent observations of the quasars 0059+581 and 0224+671. Their flux densities at 115 GHz were 1.9 and 1.1 Jy respectively. The amplitude scale was derived from measurements of 3C 454.3 and MWC 349, whose flux densities were 6.7 Jy and 1.12 Jy respectively. We estimate the final flux density accuracy to be $\sim$15%.

2.3. Merging the interferometric and single-dish observations

We used the IRAM 30–m CO $J=1\rightarrow0$ observations to derive short-spacing information and thereby complement the Plateau de Bure data. The algorithm used to derive the visibilities corresponding to each pointing centre of the mosaic is described by Gueth et al. (1996). The single-dish and interferometer visibilities are subsequently processed together. Relative weighting has been chosen to minimize the negative sidelobes in the resulting dirty beam while keeping the highest angular resolution possible. The data was processed using the GILDAS software package. A non-linear joint deconvolution of the mosaic was performed using a CLEAN-based algorithm. The images were constructed using natural weighting, and the resulting clean beam is $3.7'' \times 3.7''$.

3. Overall properties of the HH 288 outflow

3.1. Quiescent emission

The quiescent CO emission in the HH 288 region has quite complex properties. As illustrated in Fig. 2, four bright components are found in the CO $J=1\rightarrow0$ and $J=2\rightarrow1$ spectra, at about -29, -22, -17, and -8 $\mathrm{km\,s^{-1}}$, each of them having a width of $\sim$1 to 3 $\mathrm{km\,s^{-1}}$. An inspection of the channel maps shows that the corresponding emission is very extended and is unrelated to the emission of the outflowing gas. The -29 $\mathrm{km\,s^{-1}}$ component obviously corresponds to the velocity of the HH 288 exciting protostar (see below, the position-velocity diagram in Fig. 4), while the others are likely to trace unrelated foreground clouds. As expected for low-temperature optically-thin material, the CO $J=2\rightarrow1/J=1\rightarrow0$ line intensity ratio is lower than 1. The emission of all components are spatially variable in intensity (see, e.g., the similar case of NGC 2264G, Fich & Lada 1998). The -17 $\mathrm{km\,s^{-1}}$ component is actually detected only in the south-west region of our maps and only marginally overlaps the HH 288 area. The -22 $\mathrm{km\,s^{-1}}$ component shows a velocity gradient across the observed region, from -24 $\mathrm{km\,s^{-1}}$ in the southern to -20 $\mathrm{km\,s^{-1}}$ in the northern area.

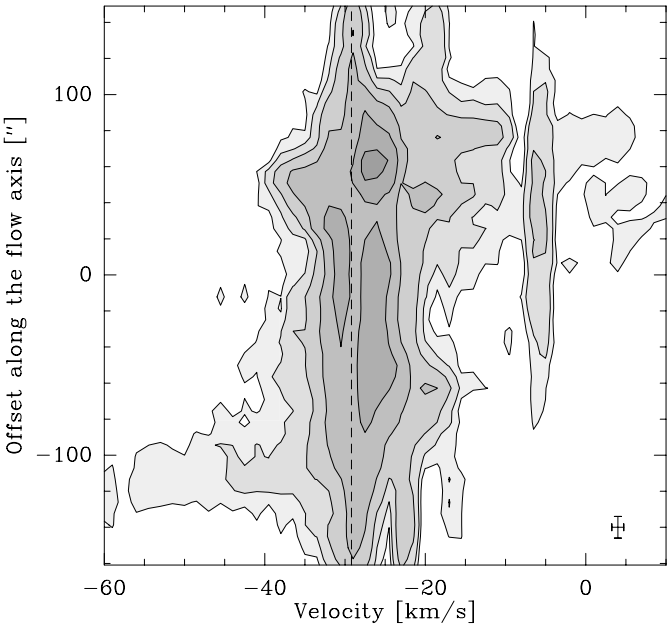

Fig. 4. Position-velocity diagram of the CO $J=2\rightarrow1$ emission along the main axis of HH 288 (labeled NS in Fig. 3a). The cross in the lower right corner represents the spatial (12″) and spectral (1.5 $\mathrm{km\,s^{-1}}$) resolutions. Contours are 2.5, 5, 10, 20, 40 and 80% of the maximum. The systemic velocity, $-29\,\mathrm{km\,s^{-1}}$, is indicated by a dash vertical line. Note the quiescent emission at about -22 and -8 $\mathrm{km\,s^{-1}}$.

3.2. Morphology and kinematics

Figure 3 presents the maps of the CO $J=2\rightarrow1$ emission in HH 288, as observed with the IRAM 30–m antenna (the angular resolution is 12″, i.e. 24 000 AU or 0.12 pc at a distance of 2 kpc). These maps reveal two well defined and highly-collimated lobes. The orientation and extent ($\sim$2 pc) of the outflow fit those of the H_2 structures, but the difference in angular resolution precludes any detailed comparison. The outflowing gas is detected at velocities of up to approximately ±35 $\mathrm{km\,s^{-1}}$. The position-velocity diagram along the flow axis (Fig. 4) reveals a somewhat confused kinematical pattern, as both lobes contain bright blue- and red-shifted emission. This can also be seen in Fig. 3b, where the overlay of the blue- and red-shifted emission maps reveals an important spatial overlap between the two lobes. This suggests that HH 288 is located very close to the plane of the sky. If only the most extreme velocities and/or the most distant emission from the protostar are considered, the blue-shifted emission shows up only in the southern lobe, while the red-shifted emission is seen only in the northern lobe. We shall therefore use this orientation in the following.

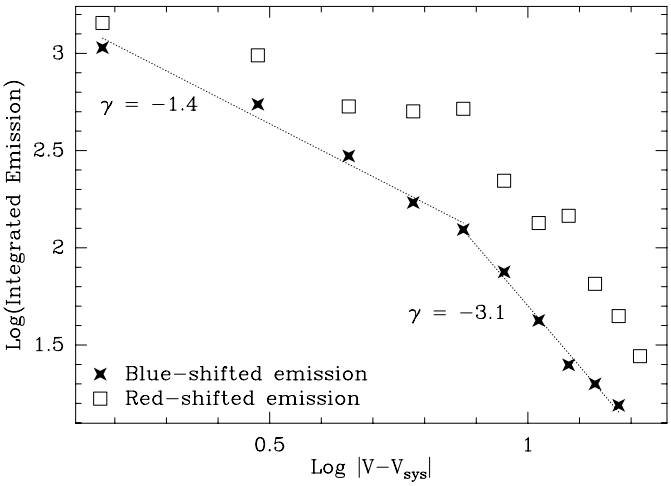

Fig. 5. Spatially integrated CO $J = 2 \rightarrow 1$ emission as a function of the velocity. Least-square fits to the blue-shifted emission (stars) are plotted as dashed lines, and the derived slopes γ are indicated. The red-shifted emission (squares) includes strong quiescent emission, and has thus not been fitted. The systemic velocity is $V_{\rm sys} = -29\,{\rm km\,s^{-1}}$.

Figure 3 shows two very interesting properties of HH 288. First, the overlap of blue- and red-shifted emission is confined to the innermost part of the outflow. In fact, each lobe seems to contain two main structures, with quite different properties: the closest from the protostar (S1 and N1 in Fig. 3b) exhibit a mixture of blue- and red-shifted emission, while the most distant (S2 and N2) have only blue- or red-shifted emission.

A second striking feature revealed by Fig. 3 is the presence of an extension almost perpendicular to the main flow axis, thus suggesting the presence of another outflow. This feature is very well seen in a few channel maps (not presented here) but also shows up in the integrated emission. It is confirmed by the interferometric maps (cf. Sect. 4) and HH 288 appears thus to be a quadrupolar outflow (e.g. Anglada et al. 1996). In the following, we shall denote these two outflows HH 288–NS and HH 288–EW, the former being the large North-South outflow (see Fig. 3a). HH 288–EW presents a simpler kinematical behaviour than HH 288–NS: the eastern lobe is clearly the blue-shifted one, while the western lobe is red-shifted (Fig. 3b).

3.3. Mass and energetics

Estimating the kinematical and dynamical parameters of HH 288 is made difficult by the strong quiescent emission observed at several red-shifted velocities, which prevent us from properly measuring the emission of the outflowing gas (see Fig. 2). An additional difficulty comes from the presence of two outflows and from the large velocity overlap between the two lobes of the main flow, making it difficult to treat each lobe separately. As a consequence, in Table 1 we present only global parameters corresponding to the whole emission, thus including the two outflows.

Table 1. Mass and energetics of the HH 288 outflows derived from the CO $J = 2 \rightarrow 1$ emission (see text). The timescale corresponds to a lobe size of 1 pc.

Typical velocity	35 $\rm km\,s^{-1}$
Timescale	2.8×10^4 y
Mass	11 $M_\odot$
Momentum	385 $M_\odot$ $\rm km\,s^{-1}$
Kinematical energy	6700 $M_\odot\,\rm km^2\,s^{-2}$
Mass flux	4×10^{-4} $M_\odot\,\rm y^{-1}$
Momentum flux ("force")	1.4×10^{-2} $M_\odot$ $\rm km\,s^{-1}\,y^{-1}$
Mechanical power	39 $L_\odot$

The CO $J = 2 \rightarrow 1$ emission was integrated from -67.5 to $7.5\,\rm km\,s^{-1}$, without taking into account the velocities at $-29 \pm 2\,\rm km\,s^{-1}$. The intensity in the velocity channels corrupted by the quiescent emission at about -22 and -8 $\rm km\,s^{-1}$ were replaced by linear interpolations of the intensities of the adjacent channels. The mass of the outflowing material was then computed assuming optically thin emission, a temperature of 30 K, and a CO/H_2 abundance of 10^{-4}. The kinematical and dynamical parameters were derived from this mass using classical relations, assuming a typical outflow velocity: we used the largest velocity of 35 $\rm km\,s^{-1}$. We refer to Cabrit & Bertout (1990) for a discussion of the advantages and drawbacks of this approach. Given the complexity of HH 288 (two outflows, several quiescent components), we stress that the values we obtain are in any case only rough estimates.

In Table 1, the mass flux $\dot{M}$ is the (mean) mass entrainment rate, as distinguished from the actual protostellar mass loss rate $\dot{M}_{\rm lost}$. If the entrainment mechanism preserves the momentum (Masson & Chernin 1992), then $\dot{M}_{\rm lost} \sim \dot{M}\,V/V_{\rm lost}$ where V is the velocity of the outflowing gas (35 $\rm km\,s^{-1}$ in Table 1) and $V_{\rm lost}$, the velocity of the ejected material. Taking $V_{\rm lost} = 200\,\rm km\,s^{-1}$ as a typical value, we derive a rough estimate of the mean mass loss rate $\dot{M}_{\rm lost} \sim 6 \times 10^{-5}$ $M_\odot\,\rm y^{-1}$.

Figure 5 presents the spatially integrated CO $J = 2 \rightarrow 1$ emission as a function of the velocity. Assuming optically thin emission, this plot directly reflects the "mass spectrum" $M(v)$ vs. v. It is now a well-established result that molecular outflows seem to be characterized by a power-law $M(v) \propto v^\gamma$ with $\gamma \sim -1.5$ to -1.8 (e.g. Richer et al. 2000; Bachiller & Tafalla 2000; see also Yu et al. 1999). Figure 5 shows a similar result for the blue-shifted emission in HH 288, the best fit giving a power-law index exponent of $\gamma = -1.4$. Interestingly, the slope steepens at the highest velocities, where the best-fit gives an exponent of $\gamma = -3.1$. Due to the confusion with quiescent emission, the red-shifted emission can barely be fitted, but it apparently shows the same behaviour. Such a departure from a single power-law has already been reported in several sources (e.g. Lada & Fich 1996; Codella & Bachiller 1999) and could result from the highest-velocity material being decelarated by the ambient gas.

Bachiller & Tafalla (2000) suggested that the break-point could possibly be used as an age indicator: the higher the velocity of the break, the younger the outflow. According to this criteria, HH 288 would then be slightly younger than the Mon R2 outflow (see Fig. 10 in Bachiller & Tafalla 2000). However, the lack of statistics, as well as projection effects, make this kind of analysis quite uncertain.

4. Internal structure of the HH 288 outflows

Figure 6 presents the channel maps of the CO $J = 1 \rightarrow 0$ emission in HH 288, resulting from the merging of the Pico Veleta and Plateau de Bure data. The angular resolution of these observations is $3.7''$, which corresponds to a linear resolution of 7400 AU (3.6×10^{-2} pc) at a distance of 2 kpc. Figure 7 presents the line-integrated emission, together with the H_2 emission and a sketch of the outflow structure described in the following section.

4.1. The HH 288–NS outflow

Southern lobe – The CO emission in the south-east lobe of HH 288–NS includes a remarkably linear structure, which seems to propagate out of the protostellar condensation position (see e.g. Fig. 7c). Although this feature is very reminiscent of a jet, our maps clearly show that it is actually only the limb-brightened western flank of a large cavity. The corresponding eastern flank appears weaker and more perturbed. The two flanks are almost parallel (see e.g. the channel map at $-34\,\mathrm{km\,s^{-1}}$) and surround the succession of faint H_2 bow-shocks (the H_2 "jet") observed along the flow axis. They are also located very precisely in the wake of the bright southern shock at the extremity of the H_2 jet (Fig. 7d), thus suggesting that the propagation of this shock played an important role in the outflow formation process. A very bright blob of CO emission is present on the flow axis, at roughly a central position in the lobe ($-19\,\mathrm{km\,s^{-1}}$). At the highest velocities ($\leq -49\,\mathrm{km\,s^{-1}}$), the CO emission is more collimated and seems to be confined along or near the flow axis. A blob of CO emission is detected at $-59\,\mathrm{km\,s^{-1}}$ (and even at larger velocities) at the extremity of the image and coincides with the strong H_2 southern bow-shock. Unfortunately, our mosaic turns out to be too small to properly map this area.

Northern lobe – The main feature of the north-west lobe of HH 288–NS is a large ovoid cavity with a clear brightness contrast between the outer and inner parts (see e.g. the channel map at $-34\,\mathrm{km\,s^{-1}}$). This cavity is obviously associated with the group of H_2 shocks located on its eastern flank (Fig. 7d). The apex shows a strong CO emission, but no clearly-defined H_2 bow-shock. The cavity is not perfectly symmetric or homogeneous: the western flank is weak while the eastern part has an extension towards the edge of the map (-29 and $-24\,\mathrm{km\,s^{-1}}$). Further downstream from this ovoid cavity, a group of bright CO blobs is present (-19 and $-14\,\mathrm{km\,s^{-1}}$) and seems to be associated with various H_2 shocks. More diffuse CO emission is observed even further away. Interestingly, high velocity ($\geq -4\,\mathrm{km\,s^{-1}}$) material elongated along the flow axis is also detected.

Flow structure – The single-dish data revealed that each lobe of HH 288–NS is made up of two main structures, with different kinematical properties (cf. Sect. 3.2). This suggests that at least two main ejection events occured at the exciting source. The interferometric maps confirm this scenario and a sketch of the corresponding outflow structure is presented in Figs. 7a and b. In the northern lobe, N1 corresponds to the ovoid cavity, while in the southern lobe S1 has a more complicated structure, including an extended emission and two bright CO blobs (Fig. 7a). Note that these two CO blobs have very well defined counterparts in the H_2 map (Fig. 7d): one of the shocks located on the axis and the bright H_2 shock in the western flank of the southern lobe. Furthern downstream from N1 and S1, evidence for a second important ejection event (N2 and S2) can be found in both lobes: N2 corresponds to the group of CO blobs already mentioned in the previous paragraph, while S2 is clearly associated with the strong H_2 shock observed in the southern lobe. However, the ejection history of HH 288–NS is certainly more complex than these two events alone, as can be inferred from the numerous H_2 and/or CO structures that are observed. The morphological differences between the northern and southern lobes could be related to the interstellar medium being denser in the northern direction (McCaughrean & Dent 2001).

Kinematics – The signal-to-noise ratio of the interferometric observations presented in this paper allows us to reconstruct images with an higher velocity resolution than that of Fig. 6. A very interesting property revealed by these maps is the kinematics of the two strong shocks (N1 and N2) observed in the northern lobe of HH 288–NS. Figure 8 presents higher velocity resolution ($1.5\ \mathrm{km\,s^{-1}}$ instead of $5\ \mathrm{km\,s^{-1}}$) channel maps of these two regions. In both cases, the same striking morphological evolution with the velocity can be observed: the CO emission is confined at the highest velocities (right panels) in a small zone near the bow apex and seems to drift along the bow surface with decreasing velocities. This is a direct observation of the velocity field of the swept-up gas in a molecular outflow. In both cases too, the apex of the CO emission coincides with a small H_2 shock, which seem thus to play a different dynamical role than other nearby H_2 features, which have no associated CO wake.

Precession? – In the first part of the flow, the brightest CO emission as well as the H_2 shocks are found in the western flank of the southern lobe and in the eastern flank of the northern lobe (see Figs. 7c and d). This property suggests that the ejection direction of HH 288–NS might be precessing (e.g. Bence et al. 1996; Gueth et al. 1996), the ejection activity occuring now in a direction slightly tilted towards the north as compared to the main axis.

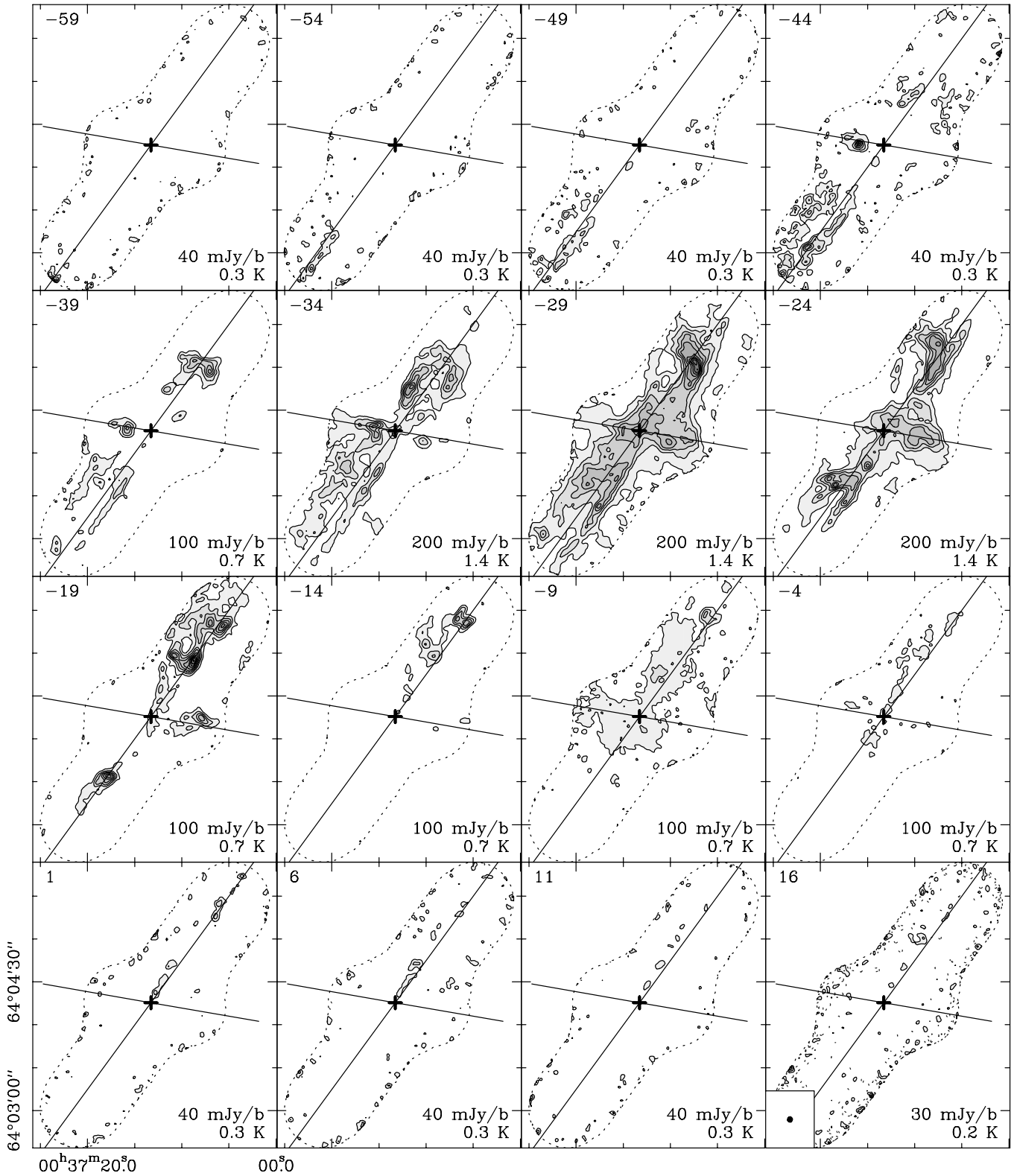

Fig. 6. Channel maps of the CO $J=1\rightarrow0$ emission in HH 288, including the short-spacing information. The emission is averaged in 5 $\mathrm{km\,s^{-1}}$ wide intervals centred on the velocities indicated in the upper left corner of each panel. The systemic velocity of HH 288 is $-29\,\mathrm{km\,s^{-1}}$. The contour spacing is *not* the same in each map and is indicated, in mJy/beam and K, in the lower right corner of each panel. The clean beam is $3.7''$. The noise rms is ∼12 mJy/beam, but strongly increases at the edges of the mosaic due to the primary beam correction. For clarity, the extent of the mosaic field of view (cf. Fig. 1) is plotted as a dotted line. The position of the central protostar and the axis of the two outflows are also drawn.

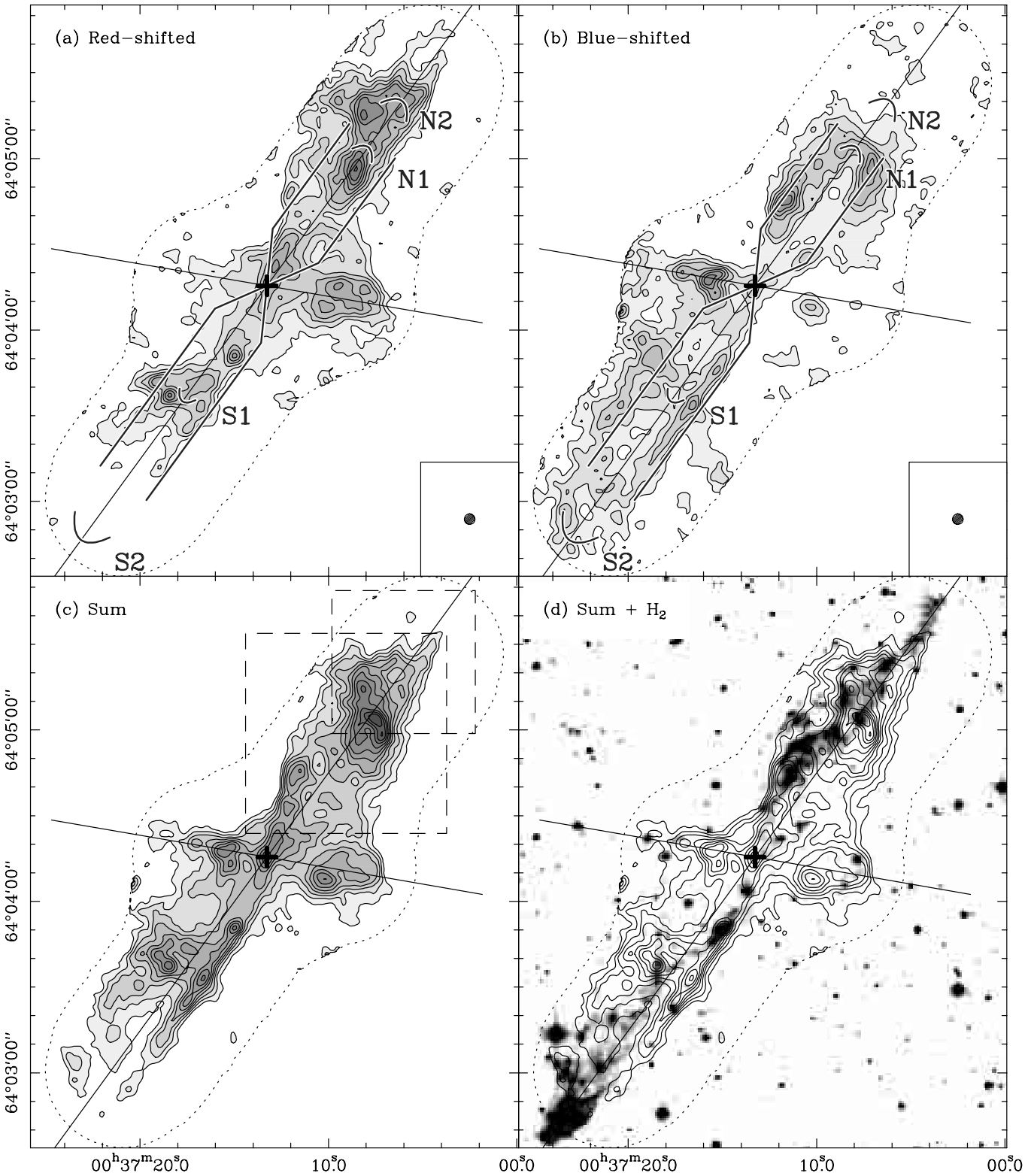

Fig. 7. Integrated CO $J=1\rightarrow0$ emission in HH 288. The clean beam is $3.7''$. **a)** Red-shifted emission, integrated from -26.5 to $22.5\,\mathrm{km\,s^{-1}}$. Contours are 1 Jy/beam $\mathrm{km\,s^{-1}}$. The first contour is not plotted. A sketch of the outflow structure is superimposed on the observations and the extent of the mosaic field of view is plotted as a dotted line. **b)** Blue-shifted emission, integrated from -76.5 to $-31.5\,\mathrm{km\,s^{-1}}$. Contours are 1 Jy/beam $\mathrm{km\,s^{-1}}$. **c)** Integrated emission for all velocities from -76.5 to $22.5\,\mathrm{km\,s^{-1}}$. Contours are 1.5 Jy/beam $\mathrm{km\,s^{-1}}$. The two first contours are not plotted, because they only show very extended structures due to quiescent emission. The two dashed boxes delineate the regions shown in Fig. 8. **d)** Overlay of the integrated CO and H_2 emission. The angular resolutions are $3.7''$ and $0.9''$, respectively.

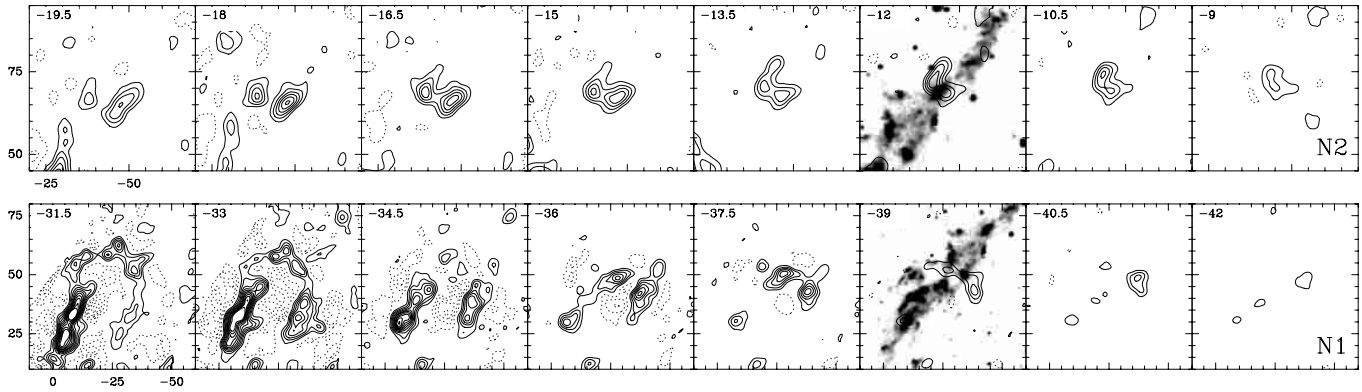

Fig. 8. Channel maps of the CO $J = 1 \rightarrow 0$ emission in two selected regions (indicated as dashed boxes in Fig. 7c) around the N1 and N2 shocks. The velocity resolution is 1.5 $\mathrm{km\,s^{-1}}$. The systemic velocity is $-29\,\mathrm{km\,s^{-1}}$. The labels of both axis are offsets from the central source, in arcseconds. Contours are 100 mJy/beam. For clarity, these images do not include the short-spacing information and the H_2 emission is plotted (greyscale) in one channel only.

The kinematical properties of N1 and S1 suggest they have a different inclination to the line of sight than the main flow, which also hints at a precession of the ejection axis: the ejection direction now would be closer to the plane of the sky. However, the complexity of the internal structure of HH 288–NS precludes us from deriving a satisfactory global description of this possible precession.

4.2. The HH 288–EW outflow

Observed with an angular resolution of $\sim 3.5''$, the HH 288–EW outflow is very well defined: two bright shocks are observed, $\sim 20''$ away from the protostellar condensation, with a clear kinematical separation between the blue-shifted eastern and the red-shifted western lobes (Figs. 6 and 7). The integrated emission shows bow-shaped morphologies, especially in the eastern shock, pointing away from the protostellar condensation. More diffuse CO emission is present between the shocks and the central source, but the presence of the HH 288–NS outflow makes it difficult to properly disentangle the emission of each flow. Interestingly, both lobes have a small collimated extension further downstream from the main shock, which, in both cases, is terminated by a faint irregular H_2 feature (Fig. 9).

The difference in orientation between the main axes of HH 288–NS and HH 288–EW is $\sim 65°$. The ratio of the projected lengths of the two flows is at least three. These numbers may of course be strongly affected by projection effects: the overall kinematical properties of the two flows suggest that HH 288–NS is closer to the plane of the sky than HH 288–EW. There is no indication of an interaction between the two flows, which would also suggest a large angle between the two axes, although the high collimation of both flows weakens this argument. In any case, the overall structure of HH 288–EW, including its apparent simplicity (as compared to HH 288–NS), does suggest that HH 288–EW is indeed smaller and younger than HH 288–NS.

The mean axes of HH 288–NS and HH 288–EW, as defined on the figures presented in this paper, intercept at the position of the central protostellar condensation (Fig. 9). It is not possible, at the resolution of these observations, to discern any difference in the origins of the two outflows. But this is also not excluded since neither axis is very precisely defined and could easily be shifted or tilted by a few arcseconds.

4.3. The exciting source: IRAS 00342+6347

The exciting source of the HH 288 outflow(s) is IRAS 00342+6347 (Dent et al. 1998). Our Plateau de Bure observations provide a map of the 115 GHz (2.6 mm) continuum emission in the HH 288 area. A 19.0 ± 1.5 mJy source is detected at the very centre of the outflow (Fig. 9) and is thus obviously associated with the exciting protostar(s). The peak is located at $\alpha = 00^{\mathrm{h}}37^{\mathrm{m}}13.27^{\mathrm{s}}$, $\delta = 64°04'15.5''$ (J2000), with a positional error of about $0.3''$. This position is in close agreement with that of the submillimetre source detected by Dent et al. (1998) with the JCMT. Although the 2.6 mm emission appears to be compact (i.e. only marginally resolved), we are most certainly not detecting a circumstellar disk, because the linear size as well as the mass (see below) are much too large as compared to known disks around low- and intermediate-mass stars (Dutrey et al. 1996; Mannings & Sargent 1997). A more likely possibility is that we are observing the inner part of the dusty envelope surrounding the protostar. Figure 9 reveals a slightly elongated structure towards the south, which could trace a part of the envelope having been perturbed by the outflow(s) (see e.g. Bachiller et al. 1995a; Gueth et al. 1997).

Figure 10 presents the spectral energy distribution (SED) of IRAS 00342+6347, including the IRAS fluxes, the 450, 800, and 1100 μm fluxes from Dent et al. (1998) and our 2.6 mm measurement. This distribution peaks in the far-infrared and is very similar to that of extremely young low-mass protostars, the Class 0 objects (see e.g. the SED of L 1448, Bachiller et al. 1995a). The bulk of

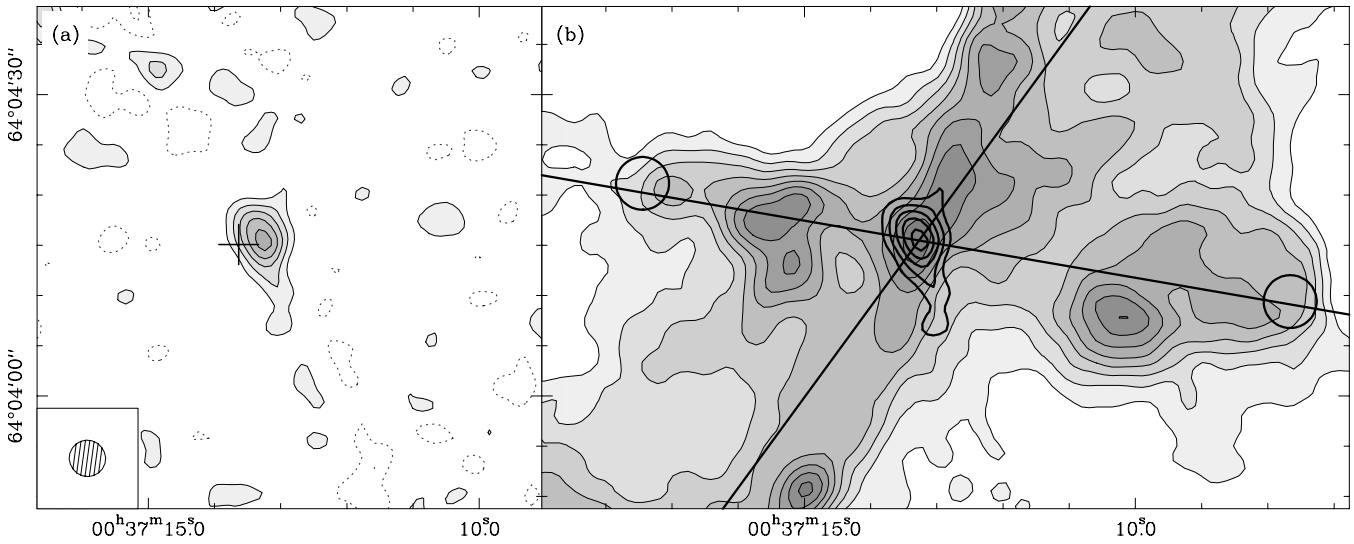

Fig. 9. a) 115 GHz (2.6 mm) continuum emission of IRAS 00342+6347. The clean beam is 3.6″. Contours are 2 mJy/beam (1.5 σ). The cross indicates the position and the corresponding uncertainty (±2″) of the submillimetre source detected by Dent et al. (1998) using the JCMT. **b)** Same image, superimposed on the integrated CO $J=1\rightarrow0$ emission (greyscale) already shown in Figs. 7c and d (same contours). The lines represent the axes of the two outflows and the circles indicate the location of the two faint H_2 features detected in HH 288–EW (see Fig. 1).

the emission is explained by the thermal emission of cold (20–50 K) dust. Pending centimetre measurements, which are not yet available, it is difficult to estimate the contribution of free-free emission to the millimetre flux densities. Note also that the 2.6 mm flux density is likely to be underestimated, because of the extended emission having been filtered out by the interferometer.

Figure 10 shows that the SED of IRAS 00342+6347 can be well fitted by a single-temperature modified blackbody (a so-called grey-body), of the form:

$$S_\nu = B_\nu(T)\,(1-\mathrm{e}^{-\tau_\nu})\,\Omega \qquad (1)$$

where B_ν is the Planck function, τ_ν the optical depth, and Ω the solid angle subtended by the source. As the flux densities plotted in Fig. 10 were measured with different instruments and thus apply to regions of different sizes, an accurate estimate of Ω is difficult. The Plateau de Bure map shows that a compact source is present, and we therefore adopted a source size of 3″. The optical depth is assumed to vary as $\tau_\nu \propto \nu^\beta$ (Hildebrand 1983). The best fit (Fig. 10) is obtained for $T \simeq 33$ K and $\beta = 2.2$. The corresponding optical depth at 1.1 mm is ∼0.06. The value of β that we derive is somewhat larger than the value $\beta \simeq 1.5$ usually adopted to describe protostellar envelopes (e.g. André & Montmerle 1994). Integrating the SED of IRAS 00342+6347, we find a bolometric luminosity of $L_{\rm bol} \sim 480\,L_\odot$, assuming a distance of 2 kpc.

Under the assumption that the emission is optically thin, the total (gas+dust) mass of the emitting region can be derived from the 2.6 mm flux density S_ν by:

$$M = \frac{S_\nu\,D^2}{B_\nu(T)\,\kappa_\nu} \qquad (2)$$

where D is the distance and κ_ν the dust mass opacity. The latter is actually poorly known and therefore introduces large uncertainties in the mass estimate (see e.g. the discussion in André & Montmerle 1994). It is usually assumed to vary as $\kappa_\nu \propto \nu^\beta$ (the same relation for τ_ν; Hildebrand 1983). Its value at 2.6 mm could range between 10^{-3} and 5×10^{-3} cm^{-2} g^{-1} (Henning et al. 1995), which yields a mass of 6 to 30 $M_\odot$ for the IRAS 00342+6347 protostellar condensation.

5. Discussion

5.1. Intermediate-mass protostars

The HH 288 exciting source (IRAS 00342+6347) is an intermediate-mass protostar, as indicated by its bolometric luminosity and envelope mass (see previous section). Its properties are very reminiscent of those of the youngest low-mass protostars, the Class 0 sources (André et al. 1993). In fact, this object would match the criteria of definition of a Class 0 source, as defined by André et al. (1993) and Barsony (1994): it is not detected at 12 μm; the ratio $L_{\rm submm}/L_{\rm bol}$, where $L_{\rm submm}$ is the luminosity radiated at wavelengths longward of 350 μm, is $\sim2\times10^{-2}$, hence larger than the defining limit of 5×10^{-3}; its SED resembles that of a cold (<40 K) black-body; and the source is driving a powerful molecular outflow. These properties indicate that IRAS 00342+6347 is an extremely young, deeply embedded intermediate-mass protostar. The estimated kinematical age of the outflow is of the order of a few 10^4 years (Sect. 3.3). Note that, as discussed below (Sect. 5.2), two protostars might be present in the IRAS 00342+6347 condensation. In that case, the bolometric luminosity and the mass that were derived in the previous section are only upper limits for each of the components. However, this does not change the order of magnitude of these parameters, and thus the overall properties of the source(s).

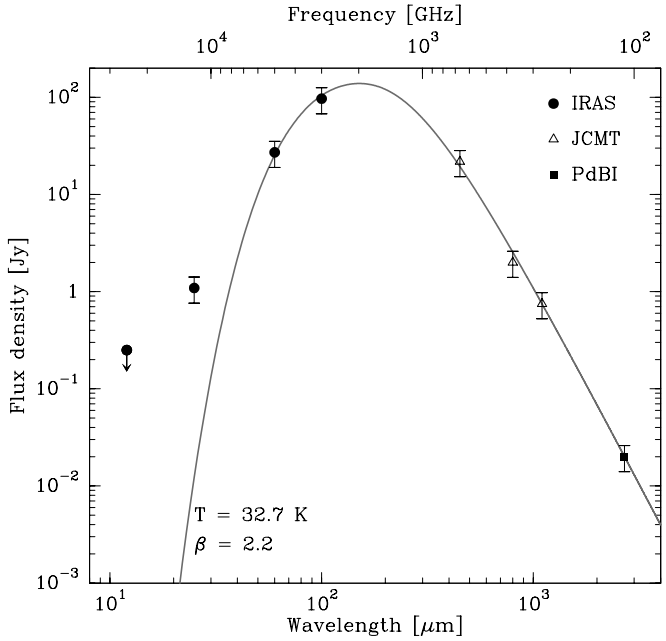

Fig. 10. Spectral energy distribution of IRAS 00342+6347. The plotted errorbars correspond to 30% of each flux density, which is a conservative estimate for IRAS as well as (sub)millimetre measurements. The solid curve is a modified black-body fitted to the data (see text). The 25 μm point was not used for the fit.

Only a very limited number of deeply embedded intermediate-mass protostars are known to date (e.g. IRAS 23011+6126 in Cep E, Lefloch et al. 1996; NGC 7129 FIRS 2, Eiroa et al. 1998; CB3-mm, Codella & Bachiller 1999). Their properties are generally rather similar to those of the low-mass Class 0 objects. A number of more evolved intermediate-mass sources (the Herbig Ae/Be stars) reveal the presence of circumstellar disks (Mannings & Sargent 1997, 2000) and are therefore thought to be the counterparts of the T Tauri stars. All these results, including those reported in this paper, suggest that the intermediate-mass star formation goes through stages qualitatively similar to the low-mass case. However, the observational and physical properties of the various steps remain largely unknown in the intermediate-mass case (see e.g. Hartmann 1999). It might therefore be premature to use the term "Class 0" for an intermediate-mass source such as HH 288, because this terminology refers to the classification of low-mass protostars, in which each step (Class 0 to Class III) is relatively precisely defined (Adams et al. 1987; André et al. 1993). It is not yet clear whether these four steps can be extrapolated to the intermediate-mass case in a straightforward manner.

5.2. HH 288: A quadrupolar outflow

A striking property revealed by the high-angular resolution maps of HH 288 is its quadrupolar morphology: two outflows are emanating from the same protostellar condensation, with a difference between the two projected axes of ∼65°. Several other sources are known to be quadrupolar, e.g. L723 (Goldsmith et al. 1984; Avery et al. 1990), Cepheus A – HW 2 (Torrelles et al. 1993), Cepheus E – IRAS 23011+6126 (Ladd & Hodapp 1997), or IRAS 20050+2027 (Bachiller et al. 1995b). To explain such quadrupolar outflows, various mechanisms have been proposed and can be classified in four categories (Anglada et al. 1996; Rodríguez 1997): *(i)* The four lobes correspond to the limb-brightened walls of a wide-angle single outflow (e.g. Avery et al. 1990). *(ii)* The interaction between an outflow and some dense interstellar material located on the flow axis deflects the outflowing gas of each lobe in two separate beams, thus creating a quadrupolar morphology (Torrelles et al. 1993). *(iii)* Two ejection events occur in the same protostellar system, but with a significant precession of the ejection direction in between (e.g. Ladd & Hodapp 1997). *(iv)* The quadrupolar outflow consists of two independent flows that are driven by two adjacent protostars (e.g. Anglada et al. 1991; Walker et al. 1993).

In the HH 288 case, the two first hypothesis can be ruled out, owing to the angular resolution provided by the interferometric observations. Indeed, the overall morphology of HH 288 does not fit into these two models: both HH 288–NS and EW include clear bow-shock structures, visible in H_2 and/or CO, and HH 288–NS presents well-defined cavities. HH 288 is clearly made up of two flows.

Can we exclude the precession scenario? Although there are some indications of a possible precession in HH 288–NS (cf. Sect. 4.1), this flow appears extremely collimated and confined along a very well defined axis. In particular, the southern lobe shows a succession of almost perfectly aligned H_2 bow-shocks. If the same protostar produced the HH 288–NS and EW outflows, this requires its ejection direction to have suddenly precessed by a very large angle. Shepherd et al. (2000) discussed the possible scenarios to produce large (>45°) precessions. The only possibility that can lead to a sudden change of the ejection direction seems to be an anisotropic accretion event, in which the (presumably massive) accretion disk is impacted by a (lower mass) condensation: in such a dramatic scenario, the disk angular momentum vector could be significantly re-oriented. We note however that the closest H_2 shocks from the protostellar condensation are located at roughly the same projected distance from the centre in the two flows. Since HH 288–NS is probably close to the plane of the sky, only HH 288–EW is likely to be affected by projection effects and its actual length is therefore larger than the observed one. Hence, the location of the shocks seems to be hardly compatible with a precession.

We therefore conclude that the simplest and thus most appealing model to explain the two ejection directions in HH 288 is the presence of two adjacent protostars in the central condensation, each one driving an independant outflow. The 2.6 mm continuum map obtained with the Plateau de Bure interferometer shows only one, unresolved source (Fig. 9), which places an upper limit of the order of 5000 AU on the projected distance between the two

suggested protostars. This is actually a very large distance compared to typical separations in pre-main-sequence binary stars (e.g. Jensen et al. 1996) and thus does not imply that the sources necessarily form a binary system. In any case, higher-angular resolution far-infrared and (sub)millimetre observations should be instrumental in assessing the nature of the exciting sources of the HH 288 flows.

5.3. Outflow formation mechanism

Our understanding of the formation process of molecular outflows mainly relies on studies of flows driven by low-mass protostars. Several models have been proposed to explain how the ejected material can transfer its momentum to the ambient molecular medium and thereby put into motion a large mass of gas (see Cabrit et al. 1997 and references therein). The two most attractive models invoke a wide-angle wind impacting a stratified ambient medium (Shu et al. 1991; Masson & Chernin 1992; Li & Shu 1996) and large bow-shocks propagating in a protostellar jet (Raga & Cabrit 1993; Masson & Chernin 1993; Chernin et al. 1994). Recent millimetre interferometric observations of several low-mass sources appear to support the shock-entrainment model (Bachiller et al. 1995a; Gueth et al. 1998; Gueth & Guilloteau 1999).

The internal structure of HH 288, as revealed by the interferometric maps presented in this paper, appears more complex than that of flows driven by low-mass protostars (e.g. HH 211, McCaughrean et al. 1994; Gueth & Guilloteau 1999; HH 212, Zinnecker et al. 1998; Lee et al. 2000) but it can still be understood, at least qualitatively, in terms of the superposition of several ejection events (cf. Fig. 7). No peculiar property was identified that could be used to infer a dynamical process different from the low-mass case. In fact, from a structural point of view, the shock-entrainment mechanism is clearly the most attractive model to explain the properties of HH 288. For instance, the southern lobe of HH 288–NS shows a cavity which is located in the wake of a large H_2 bow-shock and surrounds an H_2 jet: such coincidences strongly suggest that the propagation of the leading H_2 shock did play a dynamical role in the flow formation process. The presence of a large cavity in the northern lobe together with some more collimated material further downstream also fits into shock models (propagation of several shocks), while it seems more difficult to explain it in the framework of wind models (note, for example, that in the wind model of Li & Shu (1996), the cavity does not close back on the axis). The same argument can be invoked for HH 288–EW, in which both lobes include a main shock and, further downstream, an elongated structure terminated by an H_2 shock (see Fig. 9b).

As for the kinematics of the outflowing gas, understanding the observed velocity distribution (e.g. Fig. 8) is a complex task, because it must be determined from the intrinsic kinematics of the shock, the complex projections effects, and cumulative effects due to the propagation of the whole flow. The two first effects can be investigated using bow-shock models (Hartigan et al. 1987; Wilkin 1996; Zhang & Zheng 1997; see also Dutrey et al. 1997; Lada & Fich 1996). For instance, using the analytical solutions of Wilkin (1996) for the shape, velocity distribution and surface density of a momentum-driven bow-shock, we have computed channel maps of the column densities, i.e. of the CO emission, assuming uniform excitation temperature and optically thin emission (the corresponding position-velocity diagrams were presented in Cabrit et al. 1997). Such a model reproduces the emission being confined at the bow apex at the highest velocities as well as drifts along the bow shape with decreasing velocity. However, it differs from the observations by several aspects: the bow is too thin, which clearly results from the assumption of a geometrically thin shock layer; there is a strong emission on the axis coming from the back part of the shock (see e.g. Dutrey et al. 1997), which is not present in the observations; and the overall bow morphology does not correspond to the observed cavities, which close back on the central source position. Clearly, excitation and propagation effects are playing an important role in determining the observed CO properties. The cavity shape resulting from the propagation of a bow-shock can be computed using semi-analytical methods (Raga & Cabrit 1993; Gueth & Guilloteau 1999), but the cumulative effects on the gas kinematics are far too complex to be taken into account in such simple models.

Another approach to understand the internal structure of molecular outflows is via hydrodynamical simulations. The three-dimensional simulations of the H_2 and CO emission in molecular outflows presented by Suttner et al. (1997), Smith et al. (1997), and Völker et al. (1999) compare quite well with the HH 288 observations. In fact, the model (computed by the same group) presented by Davis et al. (1998; see their Fig. 6) shows H_2 and CO morphologies that are strikingly similar to the HH 288 southern lobe. In such simulations, the molecular outflow is formed by the swept-up gas put into motion by the propagation of the terminal bow-shock. The next step would be to produce detailed channel maps of the CO emission, in order to be compared with the whole spatio-kinematical information provided by interferometric observations.

6. Summary and conclusions

We have presented interferometric observations of the CO $J=1\rightarrow0$ emission in the HH 288 outflow, with a resolution of ∼7000 AU. Our main conclusions can be summarized as follows:

- The exciting source of the HH 288 outflow, IRAS 00342+6347, is a very young (dynamical age of the outflow ≃a few 10^4 years) intermediate-mass (bolometric luminosity ≃500 $L_\odot$, envelope mass ≃6 to 30 $M_\odot$) embedded protostar. This source closely resembles, and is therefore likely to

be an intermediate-mass counterpart of, a low-mass Class 0 object;

- The HH 288 outflow is made up of two flows, HH 288–NS and EW, with a difference of ∼65° between the position angles of the projected axes. Models which interpret such a quadrupolar morphology as the limb-brightened walls of a wide-angle single flow can be ruled out in the case of HH 288. The most appealing explanation to account for the two flows is the presence of two exciting sources in the central protostellar condensation, each one driving an independant outflow;
- Albeit complex, the internal structure of the HH 288 outflows can still be understood in terms of the superposition of two main ejection events. The comparison between the CO and H_2 emission is instrumental in such an analysis. Many features that are very often observed in low-mass protostellar outflows are also found in HH 288: highly-collimated structures, cavities or part of cavities located in the wake of H_2 shocks, bow morphologies, high-velocity material along the flow axis;
- The overall structure of HH 288, including the morphological coincidences between the CO and H_2 emission, points towards prompt entrainment at the head of travelling bow-shocks as the main flow formation process. The same mechanism would thus be at work in the outflows driven by low- and intermediate-mass protostars.

Acknowledgements. We are grateful to the IRAM staff at Pico Veleta and Plateau de Bure for competent help with the observations. This research has made use of the SIMBAD database, operated at CDS, Strasbourg, France. MJM gratefully acknowledges funding under grant No. 50 OR 0004 from the Deutsche Zentrum für Luft- und Raumfahrt.

References

Adams, F., Lada, C. J., & Shu, F. H. 1987, ApJ, 312, 788
André, P., Ward-Thompson, D., & Barsony, M. 1993, ApJ, 406, 122
André, P., & Montmerle, T. 1994, ApJ, 420, 837
Anglada, G., Estalella, R., Rodríguez, L. F., et al. 1991, ApJ, 376, 615
Anglada, G., Rodríguez, L. F., & Torrelles, J. M. 1996, ApJ, 473, L123
Avery, L. W., Hayashi, S. S., & White, G. L. 1990, ApJ, 357, 534
Bachiller, R., Guilloteau, S., Dutrey, A., Planesas, P., & Martín-Pintado, J. 1995a, A&A, 299, 857
Bachiller, R., Fuente, A., & Tafalla, M. 1995b, ApJ, 445, L51
Bachiller, R. 1996, ARA&A, 34, 111
Bachiller, R., & Tafalla, M. 2000, in The Origins of Stars and Planetary Systems, ed. C. J. Lada, & N. D. Kylafis (Kluwer Academic Press), 227
Barsony, M. 1994, in Cloud, Cores and Low Mass Stars, ed. D. P. Clemens, & R. Barvainis, ASP Conf. Ser., 65, 197
Bence, S. J., Richer, J. S., & Padman, R. 1996, MNRAS, 279, 866
Cabrit, S., & Bertout, C. 1990, A&A, 348, 530
Cabrit, S., Raga, A. C., & Gueth, F. 1997, in Herbig-Haro Flows and the Birth of Low Mass Stars, ed. B. Reipurth, & C. Bertout (Kluwer Academic Press), Proc. IAU Symp., 182, 163
Cesaroni, R., Felli, M., Testi, L., Walmsley, C. M., & Olmi, L. 1997, A&A, 325, 725
Cesaroni, R., Felli, M., Jenness, T., et al. 1999, A&A, 345, 949
Chernin, L. M., Masson, C. R., Gouveia Dal Pino, E. M., & Benz, W. 1994, ApJ, 426, 204
Churchwell, E. 2000, in The Origins of Stars and Planetary Systems, ed. C. J. Lada, & N. D. Kylafis (Kluwer Academic Press), 515
Codella, C., & Bachiller, R. 1999, A&A, 350, 659
Davis, C. J, Smith, M. D., & Moriarty-Schieven, G. H. 1998, MNRAS, 299, 825
Dent, W. R. F., Matthews, H. E., & Ward-Thompson, W. 1998, MNRAS, 301, 1049
Dutrey, A., Guilloteau, S., Duvert, G., et al. 1996, A&A, 309, 493
Dutrey, A., Guilloteau, S., & Bachiller, R. 1997, A&A, 325, 758
Eiroa, C., Palacios, J., & Casali, M. M. 1998, A&A, 335, 243
Ferreira, J., & Pelletier, G. 1995, A&A, 295, 807
Fich, M., & Lada, C. J. 1998, ApJS, 117, 147
Goldsmith, P. F., Snell, R. L., Hemeon-Heyer, M., & Langer, W. D. 1984, ApJ, 286, 599
Gómez, J. F., Sargent, A. I., Torrelles, J. M., et al. 1999, ApJ, 514, 287
Gueth, F., Guilloteau, S., & Bachiller, R. 1996, A&A, 307, 891
Gueth, F., Guilloteau, S., Dutrey, A., & Bachiller, R. 1997, A&A, 323, 943
Gueth, F., Guilloteau, S., & Bachiller, R. 1998, A&A, 333, 287
Gueth, F., & Guilloteau, S. 1999, A&A, 343, 571
Guilloteau, S., Delannoy, J., Downes, D., et al. 1992, A&A, 262, 624
Jensen, E. L. N., Mathieu, R. D., & Fuller, G. A. 1996, ApJ, 458, 312
Hartigan, P., Raymond, J., & Hartmann, L. 1987, ApJ, 316, 323
Hartmann, L. 1999, New Astron. Rev., 43, 1
Henning, T., Michel, B., & Stognienko, R. 1995, Planet. Space Sci., 43, 1333
Hildebrand, R. H. 1993, QJRAS, 24, 267
Hunter, T. R., Phillips, T. G., & Menten, K. M. 1997, ApJ, 478, 283
Lada, C. J., & Fich, M. 1996, ApJ, 459, 638
Ladd, E. F., & Hodapp, K. W. 1997, ApJ, 474, 749
Lee, C. F., Mundy, L. G., Reipurth, B., Ostriker, E. C., & Stone, J. M. 2000, ApJ, 542, 925
Lefloch, B., Eislöffel, J., & Lazareff, B. 1996, A&A, 313, L17
Li, Z. Y., & Shu, F. H. 1996, ApJ, 472, 211
Mannings, V., & Sargent, A. I. 1997, ApJ, 490, 792
Mannings, V., & Sargent, A. I. 2000, ApJ, 529, 391
Masson, C. R., & Chernin, L. M. 1992, ApJ, 387, L47
Masson, C. R., & Chernin, L. M. 1993, ApJ, 414, 230
McCaughrean, M. J., Rayner, J. T., & Zinnecker, H. 1994, ApJ, 436, L189
McCaughrean, M. J., & Dent, W. R. F. 2001, in preparation
Raga, A. C., & Cabrit, S. 1993, A&A, 278, 267
Richer, J., Shepherd, D. S., Cabrit, S., Bachiller, R., & Churchwell, E. 2000, in Protostars and Planets IV, ed. V. Mannings, A. Boss, & S. Russell (University of Arizona Press), in press

Rodríguez, L. F. 1997, in Herbig-Haro Flows and the Birth of Low Mass Stars, ed. B. Reipurth, & C. Bertout (Kluwer Academic Press), Proc. IAU Symp., 182, 83
Shepherd, D. S., & Churchwell, E. 1996a, ApJ, 457, 267
Shepherd, D. S., & Churchwell, E. 1996b, ApJ, 472, 225
Shepherd, D. S., Churchwell, E., & Wilner, D. J. 1997, ApJ, 482, 355
Shepherd, D. S., Watson, A. M., Sargent, A. I., & Churchwell, E. 1998, ApJ, 507, 861
Shepherd, D. S., Yu, K. C., Bally, J., & Testi, L. 2000, ApJ, 535, 833
Shu, F. H., Ruden, S. P., Lada, C. J., & Lizano, S. 1991, ApJ, 370, L31
Shu, F. H., Najita, J., Ostriker, E. C., & Shang, H. 1995, ApJ, 455, L155
Smith, M. D., Suttner, G., & Yorke, H. W. 1997, A&A, 323, 223
Suttner, G., Smith, M. D., Yorke, H. W., & Zinnecker, H. 1997, A&A, 318, 595
Torrelles, J. M., Verdes-Montenegro, L., Ho, P. T. P., Rodríguez, L. F., & Cantó, J. 1993, ApJ, 410, 202
Völker, R., Smith, M. D., Suttner, G., & Yorke, H. W. 1999, A&A, 343, 953
Walker, C. K., Carlstrom, J. E., & Bieging, J. H. 1993, ApJ, 402, 655
Wilkin, F. P. 1996, ApJ, 459, L31
Wouterloot, J. G. A., Brand, J., & Fiegle, K. 1993, A&AS, 98, 589
Yu, K. C., Billawala, Y., & Bally, J. 1999, AJ, 118, 2940
Zinnecker, H., McCaughrean, M. J., & Rayner, J. T. 1998, Nature, 394, 862
Zhang, Q., & Zheng, X. 1997, ApJ, 474, 719